

# Non-Destructive and Contactless Defect Detection inside Leading Edge Coatings for Wind Turbine Blades using Optical Coherence Tomography

Christian Petersen<sup>1</sup>, Søren Fæster<sup>2</sup>, Jakob Bech<sup>1</sup>, Kristine Jespersen<sup>1</sup>, Niels Israelsen<sup>1</sup>, and Ole Bang<sup>1</sup>

<sup>1</sup>Technical University of Denmark

<sup>2</sup>DTU WIND ENERGY

November 25, 2022

## Abstract

Leading edge erosion of wind turbine blades is one of the most critical issues in wind energy production, resulting in lower efficiency, as well as increased maintenance costs and downtime. Erosion is initiated by impacts from rain droplets and other atmospheric particles, so to protect the blades special protective coatings are applied to increase their lifetime without adding significantly to the weight or friction of the blade. These coatings should ideally absorb and distribute the force away from the point of impact, however, microscopic defects, such as bubbles, reduce the mechanical performance of the coating, leading to cracks and eventually erosion. In this work, Optical Coherence Tomography (OCT) is investigated for non-destructive, contactless inspection of coated glass-fiber composite samples to identify subsurface coating defects. The samples were tested using rubber projectiles to simulate rain droplet and particle impacts. The samples were subsequently imaged using both OCT, optical microscopy, and X-ray tomography. OCT scanning revealed both bubbles and cracks below the surface, which would not have been detected using ultrasonic or similar non-destructive methods. In this way, OCT can complement the existing quality control in turbine blade manufacturing, help improve the blade lifetime, and reduce the environmental impact from erosion.

## TITLE PAGE

**Manuscript title:** Non-Destructive and Contactless Defect Detection inside Leading Edge Coatings for Wind Turbine Blades using Optical Coherence Tomography

**Short running title:** OCT for defect detection in leading edge coatings

## Full name, email and author primary affiliation:

1. Christian Rosenberg Petersen (chru@dtu.dk), Department of Electrical and Photonics Engineering, Technical University of Denmark, 2800 Kgs. Lyngby, Denmark.
2. Søren Fæster (sfni@dtu.dk), Department of Wind Energy, Technical University of Denmark, 4000 Roskilde, Denmark.
3. Jakob Ilsted Bech (jakb@dtu.dk), Department of Wind Energy, Technical University of Denmark, 4000 Roskilde, Denmark.
4. Kristine Munk Jespersen (kmun@dtu.dk), Department of Wind Energy, Technical University of Denmark, 4000 Roskilde, Denmark.
5. Niels Møller Israelsen (nikr@dtu.dk), Department of Electrical and Photonics Engineering, Technical University of Denmark, 2800 Kgs. Lyngby, Denmark.

6. Ole Bang (oban@dtu.dk), Department of Electrical and Photonics Engineering, Technical University of Denmark, 2800 Kgs. Lyngby, Denmark.

**Data availability statement:** The data presented in this study is available upon request from the corresponding author. The data is not publicly available due to significant storage requirements.

**Funding statement:** This work has received funding from Horizon Europe, the European Union's Framework Programme for Research and Innovation, under Grant Agreement No. 101058054 (TURBO) and 101057404 (ZDZW). Views and opinions expressed are however those of the authors only and do not necessarily reflect those of the European Union. The European Union cannot be held responsible for them.

This work was also supported by Innovation Fund Denmark through the Grand Solutions project DURALEEDGE (8055-00012A).

**Conflict of interest disclosure:** The authors declare no conflict of interest.

**Acknowledgments:** The authors acknowledge the DURALEEDGE project partners for providing the test specimens for this work.

## RESEARCH ARTICLE

Non-Destructive and Contactless Defect Detection inside Leading Edge Coatings for Wind Turbine Blades using Optical Coherence Tomography

Christian Rosenberg Petersen<sup>1,3</sup> | Søren Fæster<sup>2</sup> | Jakob Ilsted Bech<sup>2</sup> | Kristine Munk Jespersen<sup>2</sup> | Niels Møller Israelsen<sup>1,3</sup> | Ole Bang<sup>1,3</sup>

---

<sup>1</sup>Department of Electrical and Photonics Engineering, Technical University of Denmark, 2800 Kgs. Lyngby, Denmark <sup>2</sup>Dep

---

## 1 | INTRODUCTION

The global wind energy production has been growing steadily for years as demand for clean renewable energy increase to meet global climate goals. Every year, tens of thousands of turbines are installed world-wide, which makes reliability and low-maintenance operation critical for the scalability and economic viability of wind energy production. One of the most maintenance-heavy parts are the turbine blades. In particular, the leading edge of the blade, which cuts through the air at speeds of around 300 km/h and therefore experiences the strongest forces and harshest conditions of the entire structure. Over time, collisions with rain droplets and other particles may lead to erosion, degrading the aerodynamic efficiency and thereby reducing the efficiency of the turbine. As the length and tip-speed of turbine blades have increased over the years to improve energy capacity per turbine, the challenge of controlling leading edge erosion has become increasingly difficult. One of the frontiers in this endeavor is in designing and testing durable protective coatings that can absorb and dissipate the kinetic energy from these impacts. The current industry standard for testing leading edge protection and for estimation of the coating lifetime is a liquid impingement test known as the whirling arm rain erosion test (RET) [1]. In the whirling arm test, the erosion process is simulated by spinning a blade sample inside an artificial rain field resulting in repeated droplet impacts on the leading edge. The test uses high rotational speed to accelerate the process, causing high stress loading, initiation and propagation of cracks, and eventually complete erosion of the coating. Previous studies have shown that the presence of subsurface defects reduces the mechanical performance of the coating, leading to crack formation and erosion [2,3]. Therefore, it is important to understand the correlation between manufacturing defects and the degradation of the coating performance. For characterization of RET specimens and for quality control in manufacturing of blades, a fast, non-destructive, portable, and cost-efficient scanning technology for coatings is important.

Current methods for subsurface coating inspection include high-frequency ultrasound (HFUS), THz imaging, thermographic imaging, and X-ray computed tomography (XCT). HFUS and THz has the advantage that they can penetrate all the way through the coating and into the underlying filler and composite layers.

However, due to their operation wavelength the overall spatial resolution is typically limited to the order of hundred or few hundreds microns [4,5]. In addition, HFUS requires physical contact and a coupling medium, such as ultrasonic gel, which is impractical when scanning curved surfaces. Thermographic methods infer the presence of subsurface defects from the surface thermal radiation, and as such, it is difficult to detect small or vertically stacked defects, and the results are highly dependent on the thermal properties of the sample [6,7]. XCT on the other hand can offer sub-micron imaging resolution and in principle unlimited penetration. However, the technology is limited by long processing time and the need for a rotating system to perform 3D scanning [8–10]. As such, the technique is mostly used as a laboratory technique on small cut-out samples. Furthermore, the use of ionizing radiation not only poses a risk to human health, but also a risk of damaging the sample by breaking chemical bonds and thus creating artificial defects. Another promising technology for non-destructive coating inspection is optical coherence tomography (OCT).

OCT is an interferometric imaging technique based on backscattered laser light from internal microstructures and material interfaces. It was developed in 1991 for biomedical imaging and is widely used today as a diagnostic tool within ophthalmology and dermatology [11–13]. In recent years, the technology has also found applications within non-destructive testing (NDT) due to the possibility of high resolution, non-contact 3D imaging. However, the penetration depth in many materials are severely limited by absorption and scattering, which depend on the type of material and the wavelength of the laser. Consequently, there are only a few examples in the literature where OCT has been applied for the inspection of coatings, primarily for art and cultural heritage preservation, as well as automotive and pharmaceutical coatings. Within automotive coatings, OCT systems operating around the 0.83 to 0.93  $\mu\text{m}$  central wavelength range has been used to map the thickness of individual coating layers with an axial (depth) resolution of 4–6  $\mu\text{m}$ . However, due to the short center wavelength only the top clear coat layer was transparent, limiting the maximum penetration depth to about 100  $\mu\text{m}$  [14–17]. Zhang et al. (2016) characterized automotive paints with metal flakes using OCT at 0.832  $\mu\text{m}$  and were in some cases able to distinguish the clear coat, base coat, and primer layers, each around 20–60  $\mu\text{m}$  in thickness with a depth resolution of 5  $\mu\text{m}$ . In their system, a  $2 \times 2$  mm scan of  $1536 \times 600 \times 2048$  pixels was acquired in  $\sim 45$  s and took  $\sim 60$  s to process [16]. Moving towards longer wavelengths in the mid-infrared, Cheung et al. (2015) used a broadband supercontinuum (SC) laser to compare OCT at 0.93 and 1.96  $\mu\text{m}$  central wavelength for inspection of artistic oil paintings. They found that despite the lower axial resolution of 13  $\mu\text{m}$ , the longer wavelength was able to penetrate the  $\sim 340$   $\mu\text{m}$  layer of yellow ochre pigmented paint and provide more structural information about the chalk base layer below [18]. SC lasers in particular has had a major contribution to the development of OCT, since they can provide a high spectral brightness over a broad bandwidth from ultraviolet to mid-infrared, even exceeding that of synchrotron radiation sources [19]. Using a SC laser, Zorin et al. presented improved penetration in oil paints using 4  $\mu\text{m}$  central wavelength, although with a poor axial resolution of 50  $\mu\text{m}$  and a slow line rate of 2.5 Hz [20]. Fast scanning and high-resolution in the mid-infrared was first demonstrated by Israelsen et al., most recently achieving a 3 kHz line rate and 5.8  $\mu\text{m}$  axial resolution at 4.1  $\mu\text{m}$  central wavelength [21,22]. The first study to investigate industrial coatings in the mid-infrared was by Petersen et al. that demonstrated subsurface imaging in marine coatings, including monitoring of wet film thickness during curing of a 210  $\mu\text{m}$  thickness blue-pigmented anti-fouling coating based on cuprous oxide particles, and detection of substrate corrosion through 369  $\mu\text{m}$  thickness white-pigmented high-gloss alkyd enamel [23]. In those marine coatings, the surface roughness and large functional particles presented the main limitations in terms of penetration depth.

So far, there has been no work published with OCT in relation to wind turbine and leading edge coatings. Liu et al. used OCT with a central wavelength of 1.55  $\mu\text{m}$  to monitor delamination growth in an uncoated fiber-glass epoxy composite used for the spar webs in wind turbine blades [24]. They were able to image the delamination through 2 mm of the composite material with an axial resolution of 17  $\mu\text{m}$  and a scan speed of 4 mm/s. In this work, OCT is used to non-destructively inspect coated glass-fiber composite samples to investigate the penetration depth and identify subsurface coating defects. The technique is compared with traditional XCT and optical microscopy to quantify the imaging depth and illustrate the difference in image contrast.

## 2 | MATERIALS AND METHODS

### 2.1 | Coated samples

Four coated glass-fiber composite samples were considered for testing. Three of the samples (A, B, C) were rectangular with the dimensions of 40mm x 15mm and varying thickness from 4-11 mm. The fourth sample (D) was curved, as it was cut from a model blade used for RET. The coatings on all samples were made from polyurethane (PU) and applied in varying thickness. For samples A and B, the PU coating was poured onto a horizontal composite panel to obtain a thick layer, while for C and D the coating was applied by airbrush to obtain a smooth and thin layer. Images of the samples are shown in Figure 1, and the sample characteristics are summarized in Table 1.

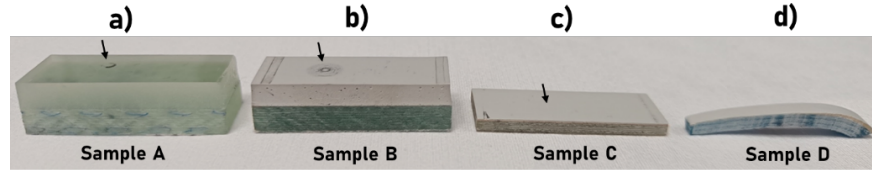


**Figure 1** (a) Photographic overview of the test samples. Arrows indicate impact sites.

**Table 1** List of sample characteristics. \*T<sub>g</sub>: Glass transition temperature.

Sample	A	B	C
Coating material	PU, clear with high T <sub>g</sub>	PU, same binder as A, light gray pigmented	Commercial PU coating, semi-
Coating thickness	~3.9 mm	~3.5 mm	~0.13 mm
Filler thickness	N/A	N/A	~0.29 mm
Sample thickness	~11 mm	~10 mm	~4 mm

### 2.2 | Impact testing

Impact tests were performed on samples A-C using an electro-pneumatic projectile launcher referred to as the Single Point Impact Fatigue Tester (SPIFT) [25]. The SPIFT was developed to repeatedly impact a target sample in a single point to be able to initiate and progress damage at high impact speeds up to 170 m/s. The purpose of the device is to mimic the impact speeds of rain droplets on the leading edge of wind turbine blades to understand the damage mechanisms of the coating materials at the relevant strain rates. Spherical nitrile rubber projectiles with a diameter of 6 mm and mass of approximately 0.1 g was used. The impacted surface was monitored continuously with a camera to observe the damage. In the current work, samples A and B were tested in the SPIFT until failure was visible on the surface, as seen in Figure 1(a,b). For sample C, the test was stopped before coating failure was visible from the surface, so only a slight difference in the shading of the coating is visible at the point of impact.

### 2.3 | X-ray CT reference scanning

XCT scanning was performed of the sample GZ3-01 for validation of the OCT images. The scan was performed on a Zeiss Xradia 520 Versa with a polychromatic X-ray beam with energies up to 60keV, generated by a tungsten target. A total of 4501 projections with an exposure time of 10 s were acquired on a 2k × 2k CCD detector during a full 360deg rotation of the sample. Density maps were reconstructed by a Feldkamp algorithm for cone beam reconstruction [26] to 3D pixel volumes with a pixel size of 9.0 μm. The standard Zeiss Xradia procedure was followed for selecting the appropriate energy and source filter to tune the X-ray energy spectrum for the sample. The reconstruction of X-ray CT data provides 3D density maps that allow detection of small density differences in the bulk material, such as the presence of crack networks

or air bubbles. Figure 2(b) shows slices from different directions through the reconstructed volume and a segmentation where air bubbles are colored blue and the cracks are red. The segmentation was made using a global intensity threshold value and visualized using Avizo 3D software for materials science.

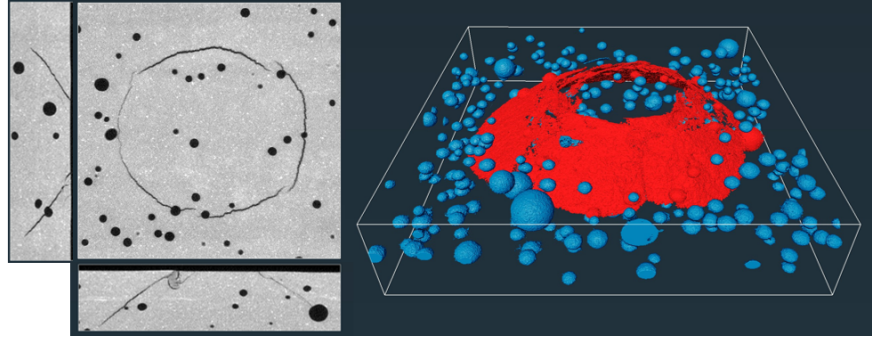


**Figure 2** XCT data and density segmentation revealing cracks (red) and air bubbles (blue) inside the coated sample B.

#### 2.4 | Optical coherence tomography systems

Two in-house-built spectral-domain OCT systems were used for imaging. The first is based on a commercial, near-infrared SC source (SuperK Extreme EXR-9, NKT Photonics) filtered around the 1.3  $\mu\text{m}$  wavelength range (1.07-1.48  $\mu\text{m}$ ). The system is able to achieve an axial (depth) resolution of around 3  $\mu\text{m}$  divided by the refractive index ( $n$ ) of the sample, and a lateral resolution of 6  $\mu\text{m}$  using a galvanometric scanning system. The system operates at a line-scan (A-scan) rate of 76 kHz with a signal sensitivity of 89 dB (amount of attenuation required to achieve a signal-to-noise ratio of one) for 4 mW average power on the sample. For more details on the system, see Ref. [12].

The second OCT system is illustrated in Figure 3(a). It is based on an in-house built SC source that covers from 1-4.5  $\mu\text{m}$ , a Michelson interferometer, a galvanometric scanning system, and an upconversion spectrometer (see ref. [21] for details). The SC output is filtered to obtain a spectrum covering 3.5-4.5  $\mu\text{m}$  with around 20 mW average power on the sample. The scanning beam is focused onto the samples using a 30 mm BaF<sub>2</sub> lens, resulting in a lateral resolution of  $\sim 30 \mu\text{m}$ . Due to the wide bandwidth of the laser, the system achieves a high axial resolution of  $\sim 8 \mu\text{m}$  (divided by the refractive index  $n$ ). The line rate of the system depends on the chosen integration time of the spectrometer, which influences the maximum imaging depth as shown in Figure 3(b). The images show a near-surface cavity in sample B with some debris inside the cavity. It is evident that the imaging depth is drastically improved when increasing the integration time from 300-1800  $\mu\text{s}$ , but only a minor improvement is obtained by doubling the integration time to 3600  $\mu\text{s}$ . This indicates that it is close to the penetration limit of the sample, given the properties of the material and the sensitivity roll-off of the OCT system [22]. For the best imaging in these highly scattering coatings, the integration time was therefore set to 3600  $\mu\text{s}$ , corresponding to a line rate of 280 Hz. A total of 400 lines were captured during a 3 mm scan, providing a cross sectional image (B-scan) roughly every 1.5 seconds with a spatial oversampling of 4. It should be noted that the depth information in OCT is obtained from the difference in optical path distance (OPD) of the sample signal relative to the stationary reference mirror path in air. Due to the refractive index of the sample, the measured OPD (and therefore the scale bar) is longer than the physical distance by a factor of  $n$ .

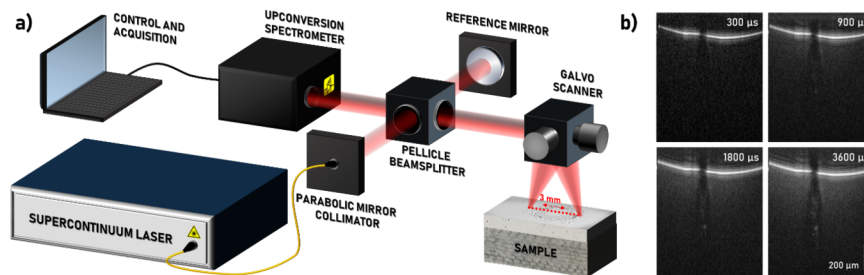


**Figure 3** (a) Experimental setup for the 4  $\mu\text{m}$  OCT system. (b) OCT imaging depth for different spectrometer integration time. The scale bar corresponds to 200  $\mu\text{m}$  assuming a refractive index of  $n=1$ .

### 3 | RESULTS AND DISCUSSION

#### 3.1 | Comparing OCT at 1.3 $\mu\text{m}$ and 4 $\mu\text{m}$

Several commercial OCT systems for imaging scattering media operate near the 1.3  $\mu\text{m}$  wavelength region. However, at 1.3  $\mu\text{m}$  the penetration depth in coatings with pigments and additives is very limited due to strong scattering from these particles [23]. Therefore, a transparent coating (sample A) was tested first using the 1.3  $\mu\text{m}$  OCT to establish a benchmark for the subsequent measurements in more realistic coatings. Figure 4(a) show a close up *en face* image (X/Y) of the impact area captured with the OCT onboard camera. The corresponding surface topography imaged using OCT is shown in Figure 4(b). It is clear from the topography of the impact site that the dark regions visible in Figure 4(a) are primarily located below the surface and therefore only visible because the coating is transparent. This becomes apparent when visualizing the OCT signal retrieved from below the surface, here visualized as an *en face* volume projection in Figure 4(c). The projection was made by superimposing individual *en face* images from just below the surface down to where the signal completely disappears. In the cross-section, additional information can be obtained about the morphology and length of the cracks. Figure 4(d) show a single B-scan, whose position is indicated by a vertical dashed line in Figure 4(b). The complex structure of the cracks can be further visualized using volume projections, as shown in Figure 4(e), which is constructed from the maximum intensity of 200 B-scans. The region of the projected volume is indicated by the horizontal dashed arrows in Figure 4(b). It is clear from the OCT images that the cracks propagate at an angle with respect to the surface, with some reaching several hundred microns in depth (divided by the refractive index of the coating). From the volume projection, there is some indication that the cracks propagate around certain areas, leaving dark voids in between. These could be formed from microscopic defects that form a cavity when exposed to the force of the impact.

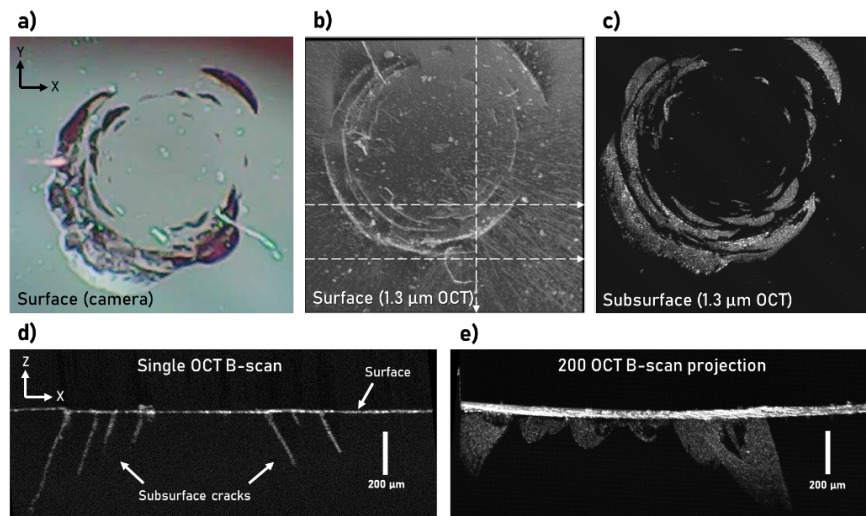


**Figure 4** OCT imaging of transparent coating sample A at  $1.3 \mu\text{m}$ . (a) Close-up en face optical image of the impact area taken with the OCT onboard camera. (b,c) OCT surface- and subsurface en face projection of the impact area, respectively. (d) Single B-scan across the impact area shown by the vertical dashed line in (b). (e) Superposition of 200 B-scans showing the patterns of cracks in the area between the horizontal dashed lines in (b). The scale bars indicate optical depth assuming of  $n = 1$ .

While imaging of subsurface cracks in the transparent coating system revealed some interesting structural patterns, it is not representative of the mechanical behavior of actual coatings with pigments and other additives. For this reason, sample B with an opaque coating system was subsequently tested using both the  $1.3 \mu\text{m}$  and  $4 \mu\text{m}$  OCT systems. A camera image of the impact region is shown in Fig. 5(a), while the corresponding OCT surface- and subsurface en face projections are shown in Figure 5(b,c) and Figure 5(e,f), respectively. The limited penetration of  $1.3 \mu\text{m}$  light in such coatings is immediately apparent from the resulting B-scan in Figure 5(g). Apart from a variation in sample orientation, the  $1.3 \mu\text{m}$  OCT subsurface projection is very similar to the camera image, while the corresponding XCT and  $4 \mu\text{m}$  OCT images in Figure 5(d) and 5(f), respectively, show the presence of a cavity near the center of the impact crater marked by an arrow and denoted (1). Due to the difference in sample orientation, the entire  $1.3 \mu\text{m}$  OCT volume was inspected, but no subsurface features could be seen. The XCT cross-section reveal that the void is located very close to the surface (around  $113 \mu\text{m}$ ), indicating that the apparent subsurface signal from the  $1.3 \mu\text{m}$  OCT image is most likely from multiple scattering, giving a false impression of the degree of penetration. This is further corroborated by the visible shadowing effect from the cracks in the  $1.3 \mu\text{m}$  OCT B-scan, while the  $4 \mu\text{m}$  OCT B-scan show that the cracks are angled as seen in the XCT image.

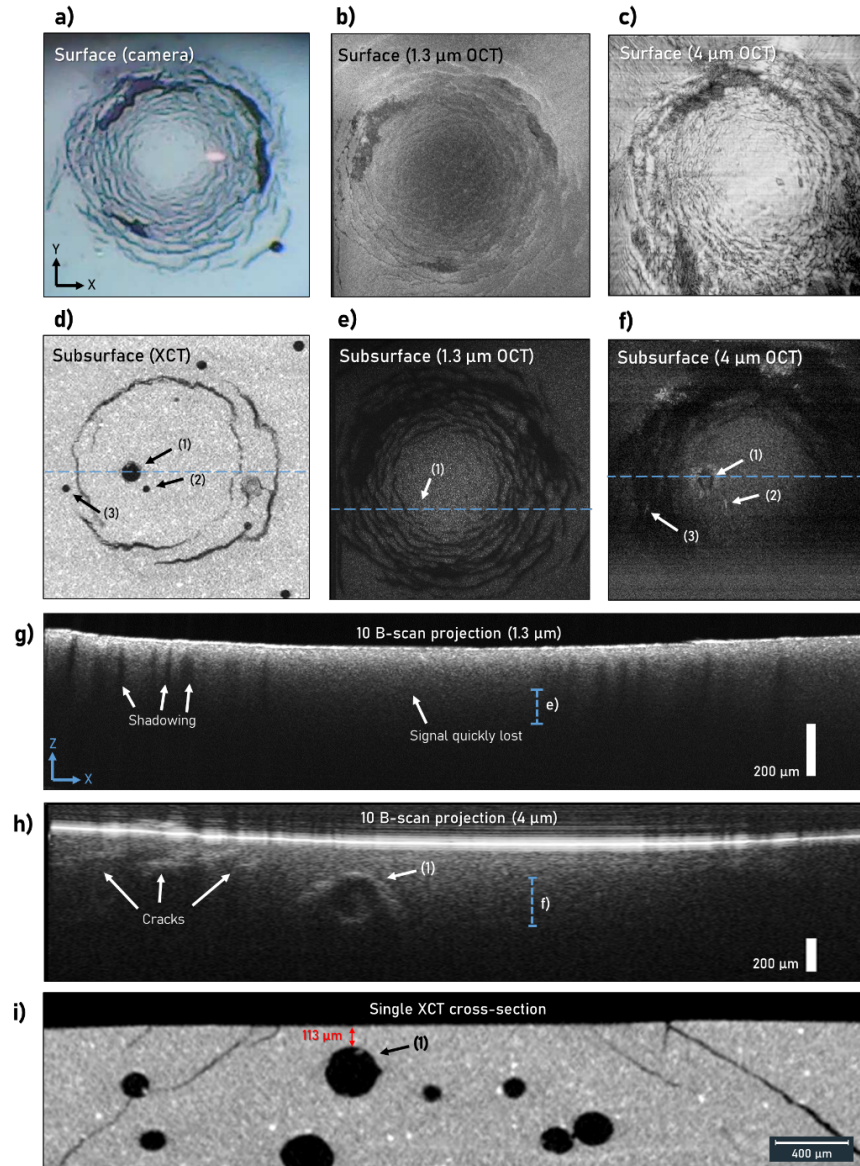


**Figure 5** OCT imaging of sample B using both 1.3  $\mu\text{m}$  and 4  $\mu\text{m}$  OCT. (a) Close-up of the impact area taken with the OCT onboard camera. (b,c) 1.3  $\mu\text{m}$  and 4  $\mu\text{m}$  OCT surface en face projection of the impact area, respectively. (d) XCT verification of subsurface voids. (e,f) 1.3  $\mu\text{m}$  and 4  $\mu\text{m}$  OCT subsurface en face projection of the impact area, respectively. Horizontal dashed lines indicate the scan positions in (g) and (h), which are offset due to different scan orientations. (g,h) Superposition of 10 B-scans using 1.3  $\mu\text{m}$  and 4  $\mu\text{m}$  OCT, respectively.

### 3.2 | Subsurface bubble detection using 4 $\mu\text{m}$ OCT and X-ray CT

In the previous section, a subsurface void was detected directly below the impact area and the observation was verified by XCT. In this section, the OCT imaging contrast and penetration depth is further compared with images obtained using XCT. Figure 6(a,c) show OCT and XCT en face images, respectively, of the surface of sample B just next to the impact. The area shows signs of strain from the impact in the top-left region, including an exposed surface bubble and a crack. The lower regions appear seemingly unaffected by

the impact. Figure 6(b,d) show the corresponding subsurface region, revealing several bubbles of varying diameter. For ease of comparison the observed bubbles are marked (1)-(5). Since the bubbles are different sizes and found at different depths, the OCT projection in Fig. 6(b) could not exclusively capture the dark air region of all bubbles simultaneously. Therefore, bubbles (2) and (4) appear as bright white spots, which marks the strong reflection from the air-coating interface at the top of the bubble. The bubbles are also clearly seen in the cross-sectional images in Figs. 6(e-j). However, compared to XCT it is clear that the penetration depth of 4  $\mu\text{m}$  OCT is still very limited. To measure the penetration depth in physical units using OCT requires knowledge of the refractive index. However, using the known 9  $\mu\text{m}$  voxel size of the XCT images a physical scale bar was generated, and from that the penetration depth could be evaluated. For example, the top and bottom of bubble (4) is located about 247  $\mu\text{m}$  and 425  $\mu\text{m}$  from the surface, respectively. The deepest point observed with OCT is the bottom of bubble (1), which is located 650  $\mu\text{m}$  below the surface, and this was only possible because of the reduced scattering inside the hollow cavity combined with a strong reflection at the air-coating interface. Still, it presents an advantage compared to ultrasonic techniques that cannot image through air. Using the known depth of bubbles (1)-(4), the refractive index of the coating was calculated to be  $n=1.59\pm 0.03$ .

Although the XCT images provide a much clearer identification of bubbles, there are other features where OCT provides a better contrast. Because the contrast of OCT is determined by reflectivity and scattering, it is sensitive to small changes in the refractive index and orientation of particles. For this reason, the OCT surface topography shown in Fig. 6(a) is much more detailed than the corresponding XCT image in Fig. 6(c). Similarly, the horizontal cracks seen in the left side of Fig. 6(i) at a similar depth to bubble (5), is not visible in the corresponding XCT image in Fig. 6(j). Only the larger crack located much deeper is seen. OCT could therefore have an advantage in detecting small cracks that have not yet opened sufficiently to be visible by XCT.

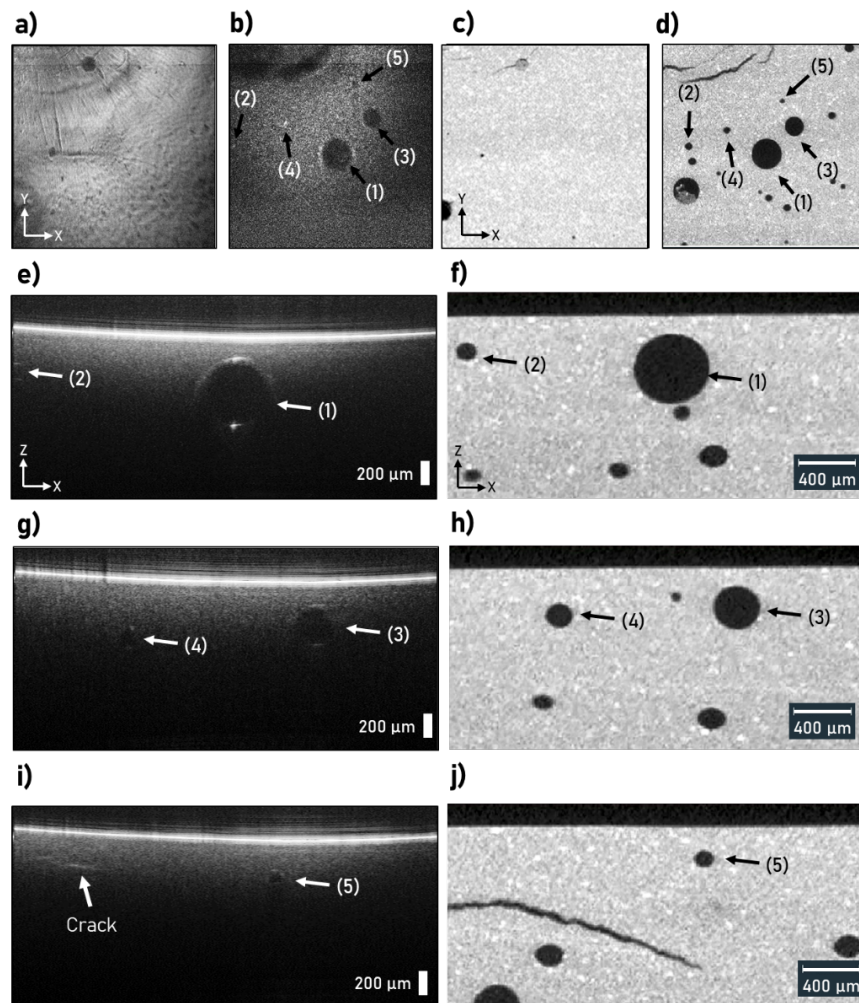


**Figure 6** Detection of sub-surface bubbles in sample B using 4  $\mu\text{m}$  OCT with XCT verification. (a,b) OCT and (c,d) XCT surface- and subsurface en face projections of the scan area, respectively. (e,g,i) OCT and (f,h,j) XCT cross-sections of bubbles (1)-(5). Note that the XCT scale is a physical scale, while the OCT scale is optical path distance (OPD) (i.e. multiplied by  $n$ ).

### 3.3 | Multilayer coatings and crack detection

Scanning sample C near the SPIFT impact region revealed no visible damage below the surface. However, it revealed how a difference in material properties can lead to a difference in the OCT image contrast. The images in the previous section were obtained from sample B, which has a single  $\sim 3.5$  mm coating layer, causing the OCT signal to slowly decay with increasing depth. However, sample C has multiple thin coating layers, as shown in the microscope image in Figure 7(c), which provides a different OCT image contrast. From the corresponding B-scan in Figure 7(d), the top coat is clearly delineated as a bright band in the image, while the second putty/filler layer show only clear signal contrast from the large filler particles. The transition from topcoat to filler is clearly seen in the corresponding line scan intensity plot in Figure 7(e). The peak at 0  $\mu\text{m}$  OPD represents the air-coating interface, while the slowly decaying signal represents the back-scattered signal from inside the coating. The change in slope at the 223  $\mu\text{m}$  mark indicates that the filler material has a significantly higher scattering coefficient, and therefore the reflected signal quickly reaches the noise level of the OCT system. The top coat of sample C also appears to have a slightly higher

scattering coefficient compared to sample B, and comparing the measured thicknesses also result in a higher refractive index of  $n = 233 \mu\text{m}/133 \mu\text{m} = 1.68$ .

It is clear that the penetration depth of OCT depends both on the system parameters, such as laser wavelength and sensitivity, as well as material properties, such as absorption and scattering coefficients. Most materials, with the exception of water, has low molecular vibrational absorption in the 3.5-6  $\mu\text{m}$  window, and since scattering in general decreases with increasing wavelength, the penetration depth could be improved by increasing the laser wavelength. However, since the axial resolution scales with  $\lambda^2/\Delta\lambda$ , increasing the wavelength also reduces the optical resolution unless a much broader spectrum is used [27]. While SC lasers covering the entire 2-10  $\mu\text{m}$  wavelength band has been demonstrated [28], it becomes increasingly challenging to find a suitable detection system that can operate in this region without lowering the detection speed or system sensitivity.

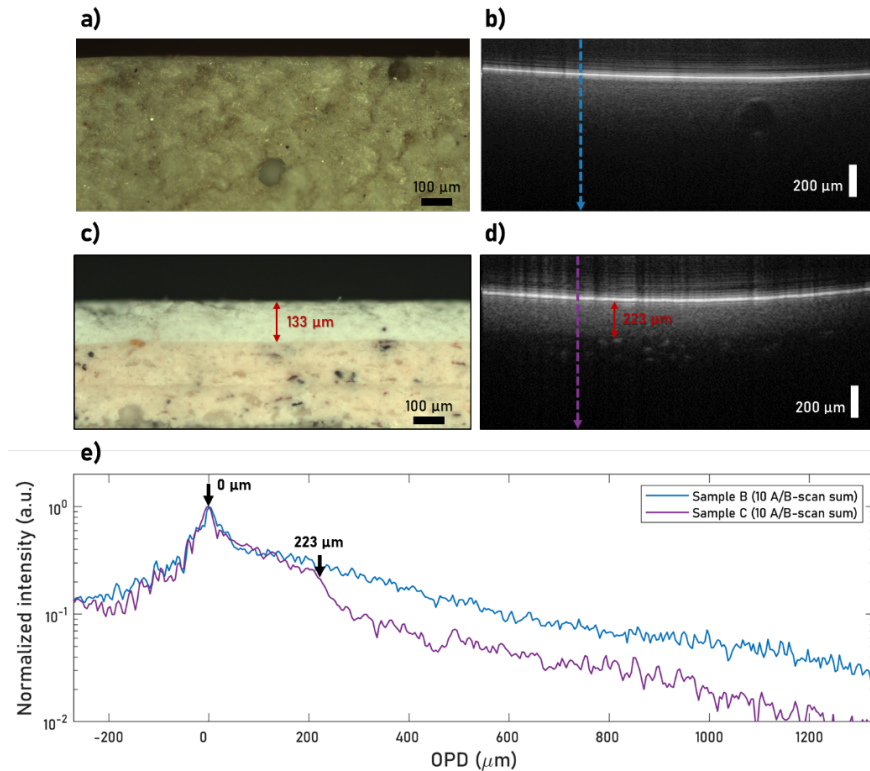


**Figure 7** (a,b) Microscope- and OCT cross-sections of monolayer sample B, respectively (not the same position). (c,d) Microscope- and OCT cross-sections of multilayer sample C, respectively (not the same position). (e) Line scan average of the two samples showing difference in scattering properties of the coating layers. The two traces represent an averaged over ten adjacent A-scans from ten consecutive B-scans, and are aligned to the strong surface reflection (0  $\mu\text{m}$  OPD). Dashed arrows in (b) and (d) indicate the line scan positions.

Figure 8 shows imaging of sample D, which had a thin PU coating deposited directly on top of the composite. The sample was cut from a larger RET blade, which appear to have initiated the formation of cracks near the edge of the cut. From the microscope image of the cut cross-section in Fig. 8(a), a bright white band clearly stands out from the rest of the composite just below the coating (marked with an arrow). Figures 8(b,e) show the surface topography and cross section along the edge of the sample, respectively. On the surface, no defects are visible, but in the cross section, two distinct features can be seen near the edge. It is clear that the features are located in the composite, since the top coating is clearly delineated. The features

marked “c” and “d” are also visualized as volume projections in Fig. 8(c) and Fig. 8(d), respectively. The cross section and volume projections together reveal that the features are not only separated in depth, but also in the lateral dimension, where “d” exactly outlines the contours of “c”. This can also be seen from the 90° rotated cross sections in Fig. 8(f,g), which represent a superposition of 10 and 20 B-scans, respectively, at the locations indicated by blue dashed lines in Fig. 8(c,d), respectively. Fig. 8(f) furthermore show that the crack at one point extend all the way to the surface through the top coating, which would likely lead to catastrophic delamination if exposed to harsh environments. A similar feature is seen at the black arrow in Fig. 8(a).

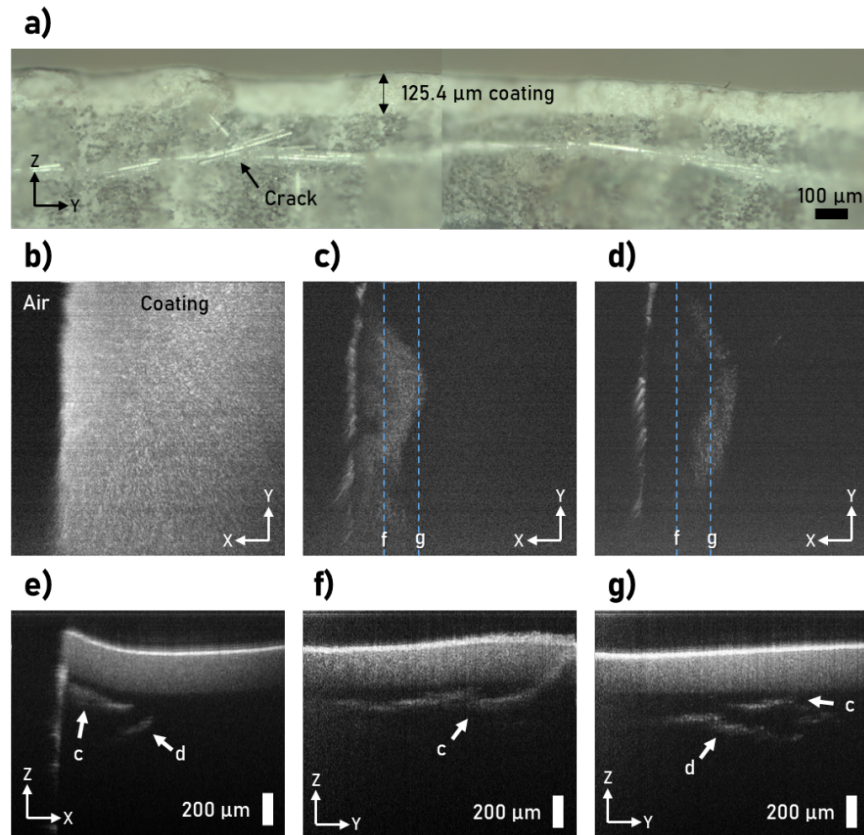


**Figure 8** Detection of cracks in cut test blade sample D. (a) Cross-sectional microscope composite image of sample D imaged along the edge of the cut (defocus due to irregular edge). Notations indicate the scale, orientation, coating thickness (double arrow), and crack (arrow). (b) OCT surface topography near the edge of the sample. (c,d) Corresponding OCT volume projections at different depths, revealing cracking along different planes. (e) B-scan near the sample edge, showing the two cracks “c” and “d” at different depths. (f,g) Cross-sections from 10 and 20 B-scans, respectively, in the same orientation as the microscope image in (a). Scan positions are indicated by the blue dashed lines in (c) and (d).

#### 4 | CONCLUSION

This work demonstrates the potential of MIR OCT as a non-destructive method for inspection of coatings on wind turbine blades. It was found that the SC laser is able to penetrate polyurethane leading edge coatings and image subsurface defects, such as bubbles and cracks below 250 μm in depth. In coatings less than 150 μm, OCT can clearly delineate the interface between different coating layers and between the coating and substrate to reveal defects and cracks. OCT is a contactless technology, that unlike ultrasound can image

through air gaps, such as cracks and bubbles. However, due to the highly scattering nature of these coatings, and especially the putty layer which has a high content of filler particles, the penetration depth of 4  $\mu\text{m}$  OCT is currently limited to imaging only very close to the surface and requires relatively long integration times on the order of milliseconds per line (seconds per B-scan) to do so. Still, there is currently no other existing non-destructive method that can image just below the surface with sufficient detail to identify coating defects. With further developments in MIR SC lasers and detector technology to increase the wavelength range and reduce the noise, the penetration depth and sensitivity of OCT is expected to improve. OCT therefore has a unique potential to complement existing methods in the quality control of coatings on wind turbine blades and RET specimens, which can contribute to improving the lifetime of turbine blades, reducing waste, and making wind energy production cheaper and more reliable.

#### ACKNOWLEDGEMENTS

The authors acknowledge the DURALEGE project partners for providing the test specimens for this work.

#### ORCID

Christian Rosenberg Petersen (0000-0002-2883-7908), Søren Fæster (0000-0001-5088-2396), Jakob Ilsted Bech (0000-0003-0228-6375), Kristine Munk Jespersen (0000-0002-6796-6200), Niels Møller Israelsen (0000-0001-9632-7902), Ole Bang (0000-0002-8041-9156).

#### REFERENCES

1. C. B. Hasager, L. Mishnaevsky, C. Bak, J. I. Bech, S. Fæster, and N. F.-J. Johansen, *How Can We Combat Leading-Edge Erosion on Wind Turbine Blades?* (Danmarks Tekniske Universitet, Institut for Vindenergi, Risø Campus, 4000, Roskilde, Danmark, 2021).
2. L. Mishnaevsky, S. Fæster, L. P. Mikkelsen, Y. Kusano, and J. I. Bech, "Micromechanisms of leading edge erosion of wind turbine blades: X-ray tomography analysis and computational studies," *Wind Energy* **23** (3), 547–562 (2020).
3. S. Faester, N. F. Johansen, L. Mishnaevsky, Y. Kusano, J. I. Bech, and M. B. Madsen, "Rain erosion of wind turbine blades and the effect of air bubbles in the coatings," *Wind Energy* **24** (10), 1071–1082 (2021).
4. C. Xu, L. He, D. Xiao, P. Ma, and Q. Wang, "A Novel High-Frequency Ultrasonic Approach for Evaluation of Homogeneity and Measurement of Sprayed Coating Thickness," *Coatings* **10**, 676 (2020).
5. I. Alig, S. Tadjbach, P. Kruger, H. Oehler, and D. Lellinger, "Characterization of coating systems by scanning acoustic microscopy: Debonding, blistering and surface topology," *Prog. Org. Coat.* **64** (2–3), 112–119 (2009).
6. Z. Qu, P. Jiang, and W. Zhang, "Development and Application of Infrared Thermography Non-Destructive Testing Techniques," *Sensors* **20**, 3851 (2020).
7. Z. Liu, D. Jiao, W. Shi, and H. Xie, "Linear laser fast scanning thermography NDT for artificial disbond defects in thermal barrier coatings," *Opt. Express* **25** (25), 31789–31800 (2017).
8. J. Zeitler and L. Gladden, "In-vitro tomography and non-destructive imaging at depth of pharmaceutical solid dosage forms," *Eur. J. Pharm. Biopharm.* **71** (1), 2–22 (2009).
9. R. S. Bradley, Y. Liu, T. L. Burnett, X. Zhou, S. B. Lyon, P. J. Withers, A. Gholinia, T. Hashimoto, D. Graham, S. R. Gibbon, and B. Hornberger, "Time-lapse lab-based x-ray nano-CT study of corrosion damage," *J. Microsc.* **267** (1), 98–106 (2017).
10. Y. Wang, J. Adrien, and B. Normand, "Porosity Characterization of Cold Sprayed Stainless Steel Coating Using Three-Dimensional X-ray Microtomography," *Coatings* **8**, 326 (2018).
11. D. Huang, E. A. Swanson, C. P. Lin, J. S. Schuman, W. G. Stinson, W. Chang, M. R. Hee, T. Flotte, K. Gregory, C. A. Puliafito, and J. G. Fujimoto, "Optical Coherence Tomography," *Science* **254** (5035),

1178–1181 (1991).

12. N. M. Israelsen, M. Maria, M. Mogensen, S. Bojesen, M. Jensen, M. Haedersdal, A. Podoleanu, and O. Bang, "The value of ultrahigh resolution OCT in dermatology - delineating the dermo-epidermal junction, capillaries in the dermal papillae and vellus hairs," *Biomed. Opt. Express* **9** (5), 2240–2265 (2018).

13. M. Mogensen, L. Thrane, T. M. Jorgensen, P. E. Andersen, and G. B. E. Jemec, "OCT imaging of skin cancer and other dermatological diseases," *J. Biophotonics* **2** (6–7), 442–451 (2009).

14. Y. Dong, S. Lawman, Y. Zheng, D. Williams, J. Zhang, and Y.-C. Shen, "Nondestructive analysis of automotive paints with spectral domain optical coherence tomography," *Appl. Opt.* **55** (13), 3695–3700 (2016).

15. C. Wang, N. Zhang, Z. Sun, Z. Li, Z. Li, and X. Xu, "Recovering hidden sub-layers of repainted automotive paint by 3D optical coherence tomography," *Aust. J. Forensic Sci.* **51** (3), 331–339 (2019).

16. N. Zhang, C. Wang, Z. Sun, H. Mei, W. Huang, L. Xu, L. Xie, J. Guo, Y. Yan, Z. Li, X. Xu, P. Xue, and N. Liu, "Characterization of automotive paint by optical coherence tomography," *Forensic Sci. Int.* **266**, 239–244 (2016).

17. J. Zhang, B. M. Williams, S. Lawman, D. Atkinson, Z. Zhang, Y. Shen, and Y. Zheng, "Non-destructive analysis of flake properties in automotive paints with full-field optical coherence tomography and 3D segmentation," *Opt. Express* **25** (16), 18614–18626 (2017).

18. C. S. Cheung, J. M. O. Daniel, M. Tokurakawa, W. A. Clarkson, and H. Liang, "High resolution Fourier domain optical coherence tomography in the 2  $\mu\text{m}$  wavelength range using a broadband supercontinuum source," *Opt. Express* **23** (3), 1992–2001 (2015).

19. C. R. Petersen, P. M. Moselund, L. Huot, L. Hooper, and O. Bang, "Towards a table-top synchrotron based on supercontinuum generation," *Infrared Phys. Technol.* **91**, 182–186 (2018).

20. I. Zorin, R. Su, A. Prylepa, J. Kilgus, M. Brandstetter, and B. Heise, "Mid-infrared Fourier-domain optical coherence tomography with a pyroelectric linear array," *Opt. Express* **26** (25), 33428–33439 (2018).

21. N. M. Israelsen, C. R. Petersen, A. Barh, D. Jain, M. Jensen, G. Hanneschläger, P. Tidemand-Lichtenberg, C. Pedersen, A. Podoleanu, and O. Bang, "Real-time high-resolution mid-infrared optical coherence tomography," *Light Sci. Appl.* **8**:11 (2019).

22. N. M. Israelsen, P. J. Rodrigo, C. R. Petersen, G. Woyessa, R. E. Hansen, P. Tidemand-Lichtenberg, C. Pedersen, and O. Bang, "High-resolution mid-infrared optical coherence tomography with kHz line rate," *Opt. Lett.* **46** (18), 4558–4561 (2021).

23. C. R. Petersen, N. Rajagopalan, C. Markos, N. M. Israelsen, P. J. Rodrigo, G. Woyessa, P. Tidemand-Lichtenberg, C. Pedersen, C. E. Weinell, S. Kiil, and O. Bang, "Non-Destructive Subsurface Inspection of Marine and Protective Coatings Using Near- and Mid-Infrared Optical Coherence Tomography," *Coatings* **11** (8), 877 (2021).

24. P. Liu, R. M. Groves, and R. Benedictus, "3D monitoring of delamination growth in a wind turbine blade composite using optical coherence tomography," *NDT E Int.* **64**, 52–58 (2014).

25. A. Fraisse, J. I. Bech, K. K. Borum, V. Fedorov, N. Frost-Jensen Johansen, M. McGugan, L. Mishnaevsky, and Y. Kusano, "Impact fatigue damage of coated glass fibre reinforced polymer laminate," *Renew. Energy* **126**, 1102–1112 (2018).

26. L. A. Feldkamp, L. C. Davis, and J. W. Kress, "Practical cone-beam algorithm," *J. Opt. Soc. Am. A* **1** (6), 612 (1984).

27. I. Hartl, X. D. Li, C. Chudoba, R. K. Ghanta, T. H. Ko, J. G. Fujimoto, J. K. Ranka, and R. S. Windeler, "Ultrahigh-resolution optical coherence tomography using continuum generation in an air-silica

microstructure optical fiber,” *Opt. Lett.* **26** (9), 608–610 (2001).

28. G. Woyessa, K. Kwarkye, M. K. Dasa, C. R. Petersen, R. Sidharthan, S. Chen, S. Yoo, and O. Bang, ”Power stable 1.5–10.5  $\mu\text{m}$  cascaded mid-infrared supercontinuum laser without thulium amplifier,” *Opt. Lett.* **46** (5), 1129–1132 (2021).

#### FIGURE LEGENDS

**Figure 1** (a) Photographic overview of the test samples. Arrows indicate impact sites.

**Figure 2** XCT data and density segmentation revealing cracks (red) and air bubbles (blue) inside the coated sample B.

**Figure 3** (a) Experimental setup for the 4  $\mu\text{m}$  OCT system. (b) OCT imaging depth for different spectrometer integration time. The scale bar corresponds to 200  $\mu\text{m}$  assuming a refractive index of  $n=1$ .

**Figure 4** OCT imaging of transparent coating sample A at 1.3  $\mu\text{m}$ . (a) Close-up en face optical image of the impact area taken with the OCT onboard camera. (b,c) OCT surface- and subsurface en face projection of the impact area, respectively. (d) Single B-scan across the impact area shown by the vertical dashed line in (b). (e) Superposition of 200 B-scans showing the patterns of cracks in the area between the horizontal dashed lines in (b). The scale bars indicate optical depth assuming of  $n = 1$ .

**Figure 5** OCT imaging of sample B using both 1.3  $\mu\text{m}$  and 4  $\mu\text{m}$  OCT. (a) Close-up of the impact area taken with the OCT onboard camera. (b,c) 1.3  $\mu\text{m}$  and 4  $\mu\text{m}$  OCT surface en face projection of the impact area, respectively. (d) XCT verification of subsurface voids. (e,f) 1.3  $\mu\text{m}$  and 4  $\mu\text{m}$  OCT subsurface en face projection of the impact area, respectively. Horizontal dashed lines indicate the scan positions in (g) and (h), which are offset due to different scan orientations. (g,h) Superposition of 10 B-scans using 1.3  $\mu\text{m}$  and 4  $\mu\text{m}$  OCT, respectively.

**Figure 6** Detection of sub-surface bubbles in sample B using 4  $\mu\text{m}$  OCT with XCT verification. (a,b) OCT and (c,d) XCT surface- and subsurface en face projections of the scan area, respectively. (e,g,i) OCT and (f,h,j) XCT cross-sections of bubbles (1)-(5). Note that the XCT scale is a physical scale, while the OCT scale is optical path distance (OPD) (i.e. multiplied by  $n$ ).

**Figure 7** (a,b) Microscope- and OCT cross-sections of monolayer sample B, respectively (not the same position). (c,d) Microscope- and OCT cross-sections of multilayer sample C, respectively (not the same position). (e) Line scan average of the two samples showing difference in scattering properties of the coating layers. The two traces represent an averaged over ten adjacent A-scans from ten consecutive B-scans, and are aligned to the strong surface reflection (0  $\mu\text{m}$  OPD). Dashed arrows in (b) and (d) indicate the line scan positions.

**Figure 8** Detection of cracks in cut test blade sample D. (a) Cross-sectional microscope composite image of sample D imaged along the edge of the cut (defocus due to irregular edge). Notations indicate the scale, orientation, coating thickness (double arrow), and crack (arrow). (b) OCT surface topography near the edge of the sample. (c,d) Corresponding OCT volume projections at different depths, revealing cracking along different planes. (e) B-scan near the sample edge, showing the two cracks “c” and “d” at different depths. (f,g) Cross-sections from 10 and 20 B-scans, respectively, in the same orientation as the microscope image in (a). Scan positions are indicated by the blue dashed lines in (c) and (d).